Computational Condensed Matter 48 (2026) e01417

Contents lists available at ScienceDirect

Computational Condensed Matter

journal homepage: www.elsevier.com/locate/cocom

Computational prediction of promising deep-UV nonlinear optical borate fluorides $SrBO_2F$ and $BaBO_2F$

Daria D. Barma [a,*], Andrey S. Obrubov [a], Abudukadi Tudi [b,c], Zhihua Yang [b,c], Anastasiia A. Mikhailova [a], Dmitry V. Rybkovskiy [a], Artem R. Oganov [a,d]

[a] Skolkovo Institute of Science and Technology, Bolshoy Boulevard 30, bld. 1, Moscow, 121205, Russia
[b] Research Center for Crystal Materials, State Key Laboratory of Functional Materials and Devices for Special Environmental Conditions, Xinjiang Key Laboratory of Functional Crystal Materials, Xinjiang Technical Institute of Physics and Chemistry, CAS, 40-1 South Beijing Road, Urumqi, 830011, China
[c] Center of Materials Science and Optoelectronics Engineering, University of Chinese Academy of Sciences, Beijing, 100049, China
[d] Sber University, Universitetskaya St. 11, Anosino village, Istra District, 143581, Russia

A B S T R A C T

The nonlinear optical performance of materials is closely related to the type and arrangement of their anionic frameworks. One-dimensional (1D) anionic frameworks exhibit strong anisotropy and facilitate the alignment of functional units. Here, two low-energy metastable borate fluorides compounds, $SrBO_2F$ and $BaBO_2F$ containing 1D $[BO_2]_\infty$ chains were predicted using the evolutionary algorithm USPEX combined with density functional theory. Both crystallize in the monoclinic non-centrosymmetric space group *C*2. Phonon and electronic structure calculations revealed a reduced dimensionality of the energy bands, with 2D and 1D dispersion relations present in the band structures. Independent-particle approximation and density functional perturbation theory calculations have shown large birefringence and second-harmonic generation coefficients comparable to KH_2PO_4. The real-space atom-cutting method revealed that the second harmonic generation of $SrBO_2F$ and $BaBO_2F$ is primarily contributed by the $[BO_2]_\infty$ infinite chains. The combination of deep-ultraviolet transparency (cut-off edge 184 nm for $SrBO_2F$ and 195 nm for $BaBO_2F$), non-centrosymmetric crystal structure, and optical anisotropy identifies $SrBO_2F$ and $BaBO_2F$ as promising candidates for DUV applications.

1. Introduction

Nonlinear optical (NLO) materials serve as the cornerstone of solid-state laser technology, enabling revolutionary advances in fields ranging from material processing to optical communication and high-resolution spectroscopy [1–3]. In particular, ultraviolet (UV) and deep-ultraviolet (DUV, $\lambda < 200$ nm) laser sources are increasingly important for applications such as water purification [4] and for phototherapy [5]. The pursuit of powerful, tunable coherent light sources in the ultraviolet (UV) and DUV regions is particularly critical, driven by the limitations of conventional excimer lasers [6].

Among inorganic materials, borates stand out as some of the most successful NLO crystals. They combine a wide optical transparency window, high laser damage thresholds, and a strong tendency to form non-centrosymmetric frameworks—an essential condition for second-harmonic generation (SHG) [7–9]. This promise is exemplified by landmark materials such as β-BaB_2O_4 (BBO) [10], celebrated for its strong nonlinearity and broad transparency. More recently, $KBe_2BO_3F_2$ (KBBF, SHG output wavelength: 165 nm); $RbBe_2BO_3F_2$ (RBBF, 180 nm); $NH_4B_4O_6F$ (ABF, 158.9 nm); $Cs_3[(BOP)_2(B_3O_7)_3]$ (199 nm); $C(NH_2)_3BF_4$ (193.2 nm) achieved coherent SHG below 200 nm [11–15], However, the technological application of KBBF is limited by the toxicity of beryllium compounds and its pronounced layer anisotropy, which hinders crystal growth. The subsequent development of $Sr_2Be_2B_2O_7$ (SBBO) has aimed to overcome these crystal growth issues while preserving optimal optical properties [16]. With the advancement of technology and industry, there is a growing need to design more high-performance DUV NLO materials.

Materials on which we are focusing contain borate and fluorine units to construct borate fluorides and fluorooxoborates, which are predicted to be capable of reducing the symmetry and thus increasing the chances of obtaining a non-centrosymmetric structure [17]. Alkaline earth (Ae) metals, particularly barium and strontium, are highly prevalent in borate crystals. A key advantage of these elements is their electronic configuration, which lacks d- or f-orbital transitions. This absence is critical, as it prevents electronic absorptions in the ultraviolet range, enabling transparency well below 200 nm. Fluorine incorporation into the B-O network has yielded a rich structural chemistry, as evidenced by such compounds as $BaB_2O_3F_2$ [18], which features unique wave-like layers containing mixed $[BO_4]$ and $[BO_3F]$ units, and the $Ae_3B_6O_{11}F_2$

* Corresponding author.
E-mail address: Daria.Barma@skoltech.ru (D.D. Barma).

https://doi.org/10.1016/j.cocom.2026.e01417
Received 25 May 2026; Received in revised form 29 July 2026; Accepted 31 July 2026
Available online 6 August 2026

(Ae = Sr, Ba) family [19]. Critically, these materials frequently crystallize in non-centrosymmetric space groups, enabling strong second-harmonic generation (SHG). For instance, $Ba_3B_6O_{11}F_2$ exhibits a large SHG response (~3 × KDP) and a deep-UV cutoff below 190 nm, while $BaB_2O_3F_2$ demonstrates an exceptionally high SHG coefficient (d_{31} = 1.57 p.m./V) and a cutoff edge as short as 175 nm. Nonetheless, other promising candidates such as $Ba_4B_{11}O_{20}F$, face challenges such as insufficient birefringence for phase matching [20]. At the same time $SrB_5O_7F_3$ demonstrates birefringence equal to 0.070 at 1064 nm and SHG response 1.6 × KDP [21].

Despite these advances, achieving a combination of strong SHG response, adequate birefringence, and DUV transparency remains a major challenge. To address this, we considered the Sr-B-O-F and Ba-B-O-F systems as a possible source of new promising DUV NLO materials and employed computational structure prediction of crystals with the $AeBO_2F$ (Ae = Sr, Ba) composition using the USPEX evolutionary algorithm, machine learning interatomic potentials and density functional theory. Our modeling allowed us to identify new low-energy metastable $SrBO_2F$ and $BaBO_2F$ borate fluoride crystals that simultaneously achieve sub-200 nm transparency, phase-matchable birefringence, and SHG coefficients exceeding 3 × KDP.

2. Computational methodology

The search of the ground state crystal structures of $SrBO_2F$ and $BaBO_2F$ materials was performed with the use of the evolutionary global optimization code USPEX [22]. The structure search and refinement were carried out in three stages.

In the first stage, global optimization was conducted for $SrBO_2F$ and $BaBO_2F$ systems with the possible number of atoms in the unit cell varying from 5 to 50. At this stage, the local optimization of structures, generated by USPEX, was performed with the Mattersim deep learning model via the Atomic Simulation Environment [23]. The use of machine learning force fields greatly speeds up the search, which is important for such complex compounds as borates.

In the second stage, the resulting $SrBO_2F$ and $BaBO_2F$ structures were collected and used as starting structures for a more accurate calculation within the projector augmented waves density functional theory method, as implemented in the VASP code [24]. To enhance the structural diversity and robustness of the global optimization, the starting set for $SrBO_2F$ was supplemented with structures of $BaBO_2F$ where Ba was replaced by Sr, and vice versa. The Perdew-Burke-Ernzerhof generalized gradient approximation was used as the exchange-correlation functional [25]. The plane-wave cutoff energy was set to 600 eV. PAW potentials were chosen as recommended by VASP developers. The valence configurations of the chosen PAW potentials were $2s^2\ 2p^1$ for B, $2s^2\ 2p^4$ for O, $2s^2\ 2p^5$ for F, $4s^2\ 4p^6\ 4d^{0.001}\ 5s^{1.999}$ for Sr and $5s^2\ 5p^6\ 5d^{0.01}\ 6s^{1.99}$ for Ba. The k-point grids were created based on the spacing between neighboring k-points equal to 0.08 $2\pi^*Å^{-1}$. Gaussian smearing of electronic occupations with a smearing width of 0.08 eV was used at this stage.

Finally, the lowest energy structures from stage 2 were collected and recalculated together with other low-energy compounds within the Sr-B-O-F and Ba-B-O-F systems to estimate their thermodynamic stability based on their height above the convex hull. We used the Materials Project database [26] as a source for known low-energy compounds. As some of these structures are known to be spin-polarized (for example, SrB_8O_{15}, $SrBO_3$, $Sr_2(BO_2)_{11}$, $Ba(BO_2)_5$), we considered spin-polarization in this final recalculation. The k-point resolution and smearing width have been changed to 0.06 $2\pi^*Å^{-1}$ and 0.05 eV, respectively.

For subsequent linear and nonlinear optical properties calculations, the unit cells of $SrBO_2F$ and $BaBO_2F$, obtained during global optimization, were converted to primitive cells with use of the SPGLIB library [27].

Linear optical properties were calculated within the independent-particle approximation (IPA) from the electronic band structure

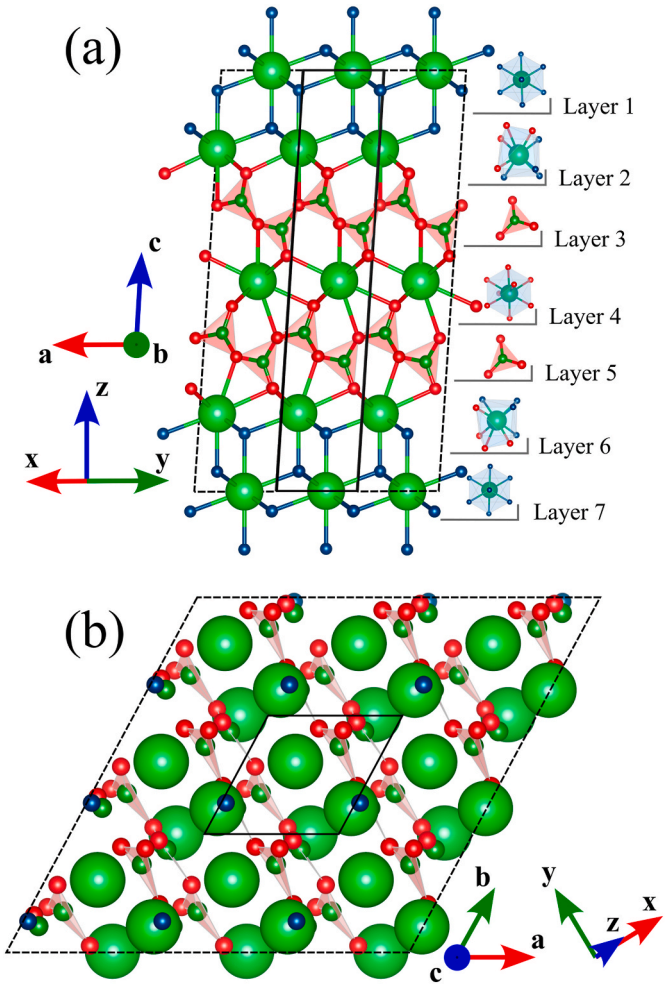

Fig. 1. Crystal structure of the predicted $BaBO_2F$, shown along the primitive directions **b** (a) and **c** (b). The Cartesian axes are also shown. The primitive unit cell is marked with black solid lines. Atoms of barium, boron, oxygen and fluorine are shown as big light green, small dark green, red and blue spheres. The coordination polyhedra, constituent the crystal, are shown next to the respective layers (a). The top-view of the primitive cell reveals the one-dimensional character of the interconnected trigonal BO_3 fragments, that are oriented along the Cartesian y-axis (b).

following the approach of Gajdoš et al. [28], as implemented in the VASP package. For these calculations, we used special versions of the PAW-potentials that were optimized for calculations requiring a large number of unoccupied states well above the Fermi level. Such potentials provide a robust description of conduction-band states and ensure the accuracy of optical spectra. During these calculations, the plane-wave cutoff energy was set to 600 eV, and the k-point grid was set equal to 18 × 18 × 4, corresponding to the k-point resolution of ~0.0143 $2\pi^*Å^{-1}$. Brillouin zone integration has been performed using the tetrahedron method with Blöchl corrections. To correct for the band gap underestimation inherent in GGA-PBE, we performed an additional electronic structure calculation using the more accurate Heyd–Scuseria–Ernzerhof hybrid functional [29].

The nonlinear optical coefficients d_{ij}, were computed using density-functional perturbation theory (DFPT) in the finite electric field with perturbation expansion after discretization (PEAD) approach as implemented in the ABINIT software [30]. The method, initially developed by Dal Corso et al. [31] has demonstrated excellent agreement with other *ab initio* methods and experimental results. It is based on the (2*n*+1) theorem, which allows to compute third order energy derivatives knowing only ground-state energy and first-order wave functions [32].

Optimized Norm-Conserving Vanderbilt (ONCV) pseudopotentials were used for calculations [33]. For both $SrBO_2F$ and $BaBO_2F$, the plane-wave cut-off energy was chosen equal to 40 Hartree and the k-point resolution was set to 0.02 $2\pi^*Å^{-1}$.

Phonon calculations were carried out using density functional perturbation theory as implemented in Quantum ESPRESSO software [34]. The same ONCV pseudopotentials [33] were used for the description of electron-ion interaction. Exchange and correlation were treated within the GGA-PBE functional. The plane-wave kinetic energy cutoff of 80 Ry and a 4 × 4 × 1 k-point grid were used for the self-consistent field procedure. Before the phonon calculations, the geometries of the investigated structures were reoptimized. After the geometry optimization, the dynamical matrices were computed on a uniform 4 × 4 × 2 q-point grid. The interatomic force constants were obtained via Fourier transformation and used to calculate phonon dispersion relations along high-symmetry directions in the Brillouin zone. The calculation of phonon densities of states was performed on a dense 24 × 24 × 6 q-point grid.

3. Results and discussion

The evolutionary structure search revealed similar lowest-energy crystal structures for both $SrBO_2F$ and $BaBO_2F$ compounds. Both compounds are found in space group *C*2 of the monoclinic system and contain 4 formula units in their primitive cells. The crystal structures in CIF format and primitive cells in POSCAR format for both structures are given in the Supplementary Information. The structure of $BaBO_2F$ is shown in Fig. 1. It features $[BO_2]_\infty$ chains of corner-sharing BO_3-triangles and Ba (or Sr) atoms in a distorted cubic coordination (forming AeO_8, AeF_8 and AeO_4F_4 cubes).

Alternating layers (Fig. 1(a)) are clearly distinguished.

1. Layers 1 and 7 contain AeF_8 cubes—the most symmetric units in the structure, since all vertices are occupied by fluorine atoms. The Me–F bond length ranges from 2.69 to 2.7 Å.
2. Layers 2 and 6 consist of mixed AeO_4F_4 polyhedra. The reduction in symmetry relative to layer 1 (7) arises from partial substitution of fluorine by oxygen, which possesses a slightly larger ionic radius. The Ae–F bond lengths are 2.69–2.73 Å, and the Ae–O bond lengths are 2.74–2.87 Å.
3. Layers 3 and 5 are composed of interconnected trigonal BO_3 fragments tilted by approximately 18.40° with respect to each other. These groups share oxygen atoms to form $[BO_2]_\infty$ chains repeating along the Cartesian y-axis. The B–O bond lengths are 1.42, 1.40, and 1.34 Å.
4. Layer 4 features AeO_8 polyhedra. The symmetry reduction compared to AeF_8 is attributed to the absence of coupling with the buffer layer AeO_4F_4 and to direct contact with the BO_3 layer, which induces a moderate distortion of the polyhedron.

It is worth contrasting the $[BO_2]_\infty$ chain architecture formed by the corner-sharing BO_3 triangles of layers 3 and 5 with the anionic framework of the benchmark KBBF structure. In KBBF, BO_3 groups are covalently linked within each layer into a near-planar two-dimensional Be_2BO_3 network, but adjacent layers interact only weakly, which has been identified as the structural origin of the pronounced layer growth habit that hinders large-crystal growth. A strategy of suppressing this layered growth habit by strengthening the connectivity between layers (or structural fragments) has been successfully implemented in the more recently reported $(NH_4)_3B_{11}PO_{19}F_3$ (ABPF) [35], where strong B–O–P covalent linkages connect the $[B_5PO_{10}F]_\infty$ layers and were shown to mitigate the limitations of the KBBF-type layered habit. In $SrBO_2F$ and $BaBO_2F$, the individual BO_3 triangles are oriented approximately perpendicular to layers 2 (6) and 4 – in direct contrast to KBBF, where the BO_3 plane normal is parallel to the stacking axis, keeping each triangle confined within its layer. Consecutive triangles along the $[BO_2]_\infty$ chain are additionally tilted by ~18.4° with respect to each other (Fig. 1), producing a zigzag chain geometry. This near-perpendicular orientation naturally brings the chain oxygen atoms into direct contact with the coordination polyhedra of the adjacent Sr/Ba-containing layers, providing three-dimensional connectivity across the stack, in contrast to the coplanar, layer-confined BO_3 network of KBBF. This direct interlayer linkage is structurally analogous in spirit to the interlayer-bridging strategy noted above for ABPF, and may likewise offer a route to reduced growth anisotropy compared to KBBF-type materials.

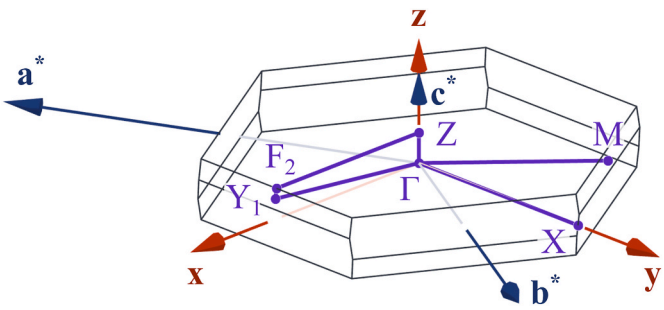

Fig. 2. First Brillouin zone of $BaBO_2F$. Dark blue arrows depict the reciprocal lattice vectors; red arrows show the Cartesian axes. High-symmetry points and lines between them illustrate the path for the band structure calculations.

The first Brillouin zone of $BaBO_2F$ is shown in Fig. 2 (the figure is plotted with use of the Brillouin.jl [36] package for the Julia programming language). The coordinates of high-symmetry points, which will be further used for band structure calculations are: X=(−0.339, 0.339, 0), Γ=(0, 0, 0), Y_1=(0.5, 0.5, 0), F_2=(0.496, 0.496, 0.168), Z=(0, 0, 0.5), M=(−0.5, 0, 0.5). For $SrBO_2F$ the coordinates are the same except for X and F_2: X=(−0.350, 0.350, 0), F_2=(0.496, 0.496, 0.156).

The thermodynamic stability of the obtained crystals was estimated based on the heights of their formation energies above the convex hull. Our results indicate that both predicted phases are very close to the convex hull, only 7 meV/atom and 6 meV/atom above for $SrBO_2F$ and $BaBO_2F$, respectively. These values can be compared with those of the experimentally observed borates and borate fluorides with similar compositions. Some of such materials lie exactly on the convex hull, like the isostructural compounds $Sr_3B_6O_{11}F_2$ and $Ba_3B_6O_{11}F_2$, which have been characterized as promising for nonlinear optics (d_{11} = 1.39 p.m./V and d_{11} = 1.58 p.m./V respectively) [19]. But at the same time experimentally observed borate fluorides such as $NaBe_2BO_3F_2$ (d_{11} = 0.74 p.m./V) and $BaY_6(Si_3B_6O_{24})F_2$ (d_{33} = 4.61 p.m./V) have similar energies above the convex hull equal to 6 meV/atom and 8 meV/atom, respectively [37,38]. The experimentally observed borate SrB_4O_7 [39] is also 7 meV/atom above the convex hull. Therefore, the predicted low-energy metastable phases have potential for synthesis under nonequilibrium conditions or via targeted doping.

To investigate the dynamical stability of the predicted compounds, we calculated the phonon frequencies across the first Brillouin zone in frames of DFPT. The resulting phonon band structures, calculated along the high-symmetry path X-Γ-Y_1-F_2-Z-Γ-M in reciprocal space, together with the projected and total densities of phonon states, are shown in Fig. 3. The absence of imaginary frequencies indicates the dynamical stability of $SrBO_2F$ and $BaBO_2F$ (minor negative frequencies with a magnitude of ~ -2 cm^{-1} around Γ are attributed to numerical inaccuracies). The phonon band structures of both materials are very similar. The displacements of metal atoms contribute mostly to the phonon states with frequencies below ~200 cm^{-1}. Fluorine has the strongest contribution to states below ~350 cm^{-1}. The displacements of boron and oxygen atoms are presented in the entire frequency range. The states above ~350 cm^{-1} have the highest contributions from B and O. Most of these states are remarkable due to their clearly reduced dimensionality, which is expressed in almost absent dispersion in Γ-Z, Γ-Y_1 and F_2-Z

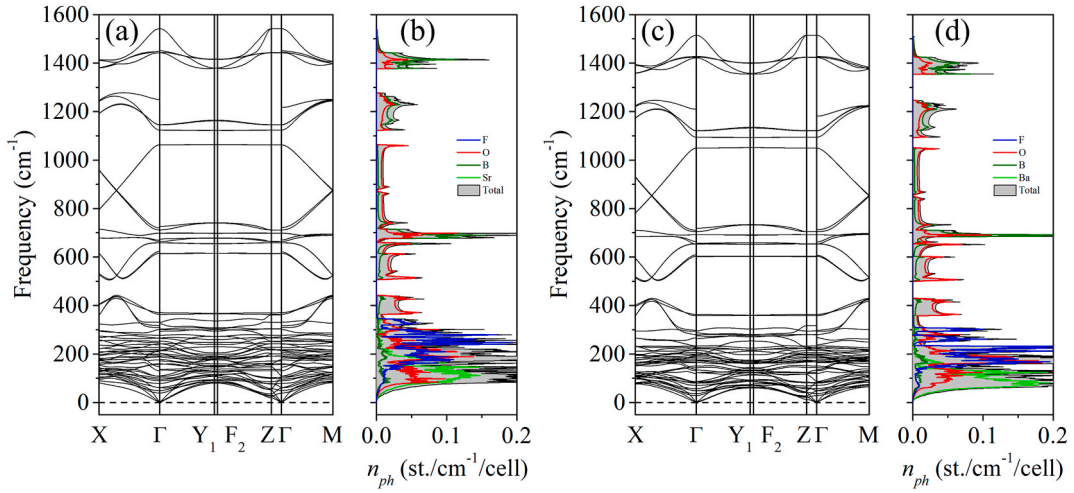

Fig. 3. Phonon band structures and projected densities of states n_{ph} for $SrBO_2F$ (a, b) and $BaBO_2F$ (c, d).

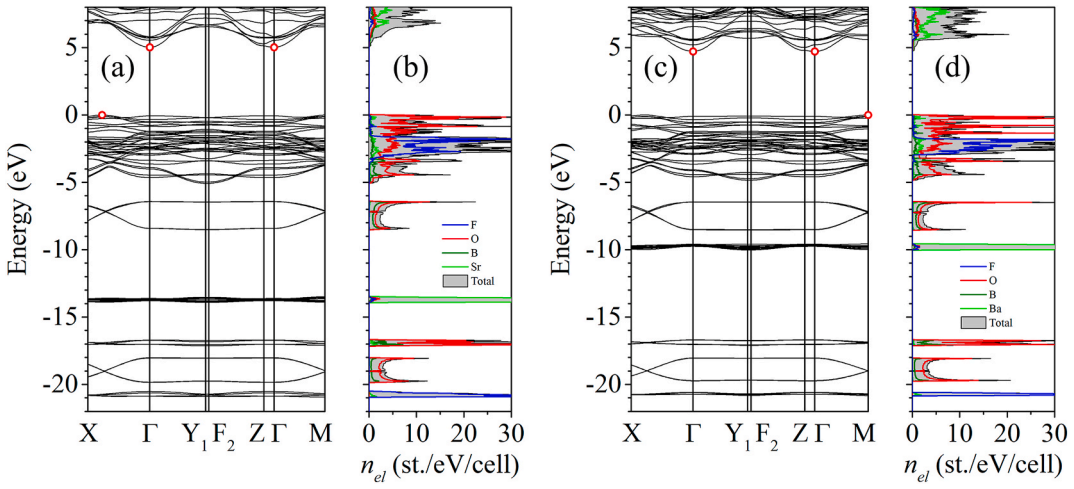

Fig. 4. Electronic band structures and projected densities of states n_{el} for $SrBO_2F$ (a, b) and $BaBO_2F$ (c, d), calculated within the PBE functional. Lower-lying 4s-bands of Sr and 5s-bands of Ba are not shown. The energy origin adjusted to the top of the valence band. Band extrema of the highest valence band and lowest conduction band are marked with open red circles.

directions. Such band shape makes these phonon bands effectively one-dimensional, which is a consequence of the specific feature of the crystal structures, where $[BO_2]_\infty$ chains are oriented along the Cartesian y-axis and have considerable separation between each other along the x- and z-axes. Another feature worth mentioning is the LO-TO splitting of some phonon bands near the Γ point, which is common for polar materials. The longitudinal optical (LO) mode's ionic motion creates a macroscopic depolarizing electric field that adds an extra restoring force on the ions, stiffening their vibration and raising the LO frequency. In contrast, the transverse optical (TO) phonon produces no such net field and thus stays at the lower, unsplit frequency. For the predicted materials this effect is particularly strong for states between ~1100 and ~1250 cm^{-1} around Γ.

Next, we turned to the investigation of the electronic subsystem of the predicted materials. The energies of the electronic bands of $SrBO_2F$ and $BaBO_2F$ were calculated along the same high-symmetry paths as the phonon bands. The resulting electronic band structures, together with the projected density of states (PDOS), calculated within the PBE functional, are shown in Fig. 4 (it is worth noting that, due to peculiarities of the DOS projection method implemented in VASP, the partial DOS does not always sum up to the total DOS). The band structures of both materials are quite similar. Most of the electronic bands have only weak dispersion along the Γ-Z direction (in the direction perpendicular to the atomic layer planes). The electronic structures of both materials have, therefore, a strongly two-dimensional character. The valence bands can be divided into several groups. The first group, located between 0 eV and −5 eV, consists of multiple hybridized orbitals with the contributions from *2p* orbitals of oxygen and fluorine. Two similar groups of bands, located at energy ranges between −6.5 and −8.5 eV and −18 and −20 eV, are composed mainly of oxygen and boron *2p* (for higher energies) and *2s* (for lower energies) orbitals. Interestingly, besides the abovementioned lack of dispersion along the Cartesian z-axis, these bands are also almost flat along the Γ-Y$_1$ and F$_2$-Z directions in the first Brillouin zone. This reduces the dimensionality of these two groups of bands further from 2D to 1D, with only considerable band curvature along the Γ-X direction. The one-dimensional character of these bands is also reflected in the shape of the corresponding densities of states that have a well-pronounced 1D-character with sharp Van Hove singularities at the band edges. As in the case of the phonon band structure, the reduced dimensionality of these electron bands is explained by the one-dimensional structure of the $[BO_2]_\infty$ chains. The very narrow groups of bands, composed of *p* orbitals of metal atoms, are located at ~ -14 eV for $SrBO_2F$ and ~-10 eV for $BaBO_2F$. The remaining two, also very narrow groups of bands, are mainly attributed to *2s* orbitals of oxygen (at ~ -17 eV) and fluorine (at ~ -21 eV). The lowest conduction bands exhibit

generally higher dispersion and have the largest contributions from *5s* orbitals of Sr and *6s* orbitals of Ba. The topmost valence band is relatively flat, and the valence band maximum is located between the X and Γ points for $SrBO_2F$ and at the M-point for $BaBO_2F$. The bottom of the conduction band is positioned in the Brillouin zone center in both cases. The lowest energy gap, calculated within the PBE functional, is therefore indirect in both materials and is equal to 5.02 eV for $SrBO_2F$ and 4.72 eV for $BaBO_2F$. The smallest direct gap in both materials is located at the Γ-point and is equal to 5.08 eV for $SrBO_2F$ and 4.82 eV for $BaBO_2F$.

It is well known, however, that the PBE functional tends to underestimate the band gap values. To introduce a correction to the band gap for further calculation of optical properties, we performed another electronic structure calculation with use of the HSE06 hybrid functional, whose band gap values are in better agreement with experiment. The resulting direct (indirect) band gaps were obtained equal to 6.78 (6.73) eV and 6.45 (6.35) eV for $SrBO_2F$ and $BaBO_2F$, respectively.

Both indicated candidates were investigated in terms of their optical and nonlinear optical properties. Among the linear optical properties, it was especially important to calculate the birefringence value for the achievement of the phase matching condition and phase matching wavelength in order to determine the possible range of wavelengths of the second harmonic wave.

To obtain the birefringence and the shortest phase matching wavelength, we first calculated the frequency-dependent dielectric tensors. A scissor shift was applied to the band gap to account for the difference between PBE and the more accurate HSE06 functional. The birefringence was then determined as the difference between the largest and smallest refractive indices at the specific wavelength of 1064 nm — a common choice in optical applications. Birefringence values were calculated to be equal to 0.087 and 0.077 for $SrBO_2F$ and $BaBO_2F$, respectively. The optimal value of birefringence for achieving phase synchronism is considered to be not less than 0.05, meaning that both materials have promising values of this parameter. Then the phase matching wavelength was determined as the cross point of refractive index functions depending on initial and double frequency [40]. The lowest-wavelength phase matching values were evaluated as equal to 197 nm and 222 nm for $SrBO_2F$ and $BaBO_2F$, respectively, making the former somewhat more suitable for the DUV spectrum range.

The main parameter of nonlinear optical materials, second harmonic generation (SHG) coefficients, were calculated within DFPT. The obtained coefficients *d*, in units of pm/V, written in Voigt notation are:

$$\boldsymbol{d}_{SrBO_2F} = \begin{bmatrix} 0.000 & 0.000 & 0.000 & 0.002 & 0.000 & -0.036 \\ -0.036 & -1.161 & 1.029 & 0.000 & 0.002 & 0.000 \\ 0.000 & 0.000 & 0.000 & 1.029 & 0.000 & 0.002 \end{bmatrix}$$

$$\boldsymbol{d}_{BaBO_2F} = \begin{bmatrix} 0.000 & 0.000 & 0.000 & 0.004 & 0.000 & -0.088 \\ -0.088 & -1.166 & 1.095 & 0.000 & 0.004 & 0.000 \\ 0.000 & 0.000 & 0.000 & 1.095 & 0.000 & 0.004 \end{bmatrix}$$

The values of second harmonic generation coefficients are considered high enough if they are at least comparable to d_{36} (0.384 p.m./V) of KDP (KH_2PO_4) crystal [41,42]. Comparing the largest components with KDP we get:

for $SrBO_2F$:

$$\left|d_{22}^{SrBO_2F}\right| = 3.02 \times KDP,$$

$$\left|d_{23}^{SrBO_2F}\right| = \left|d_{34}^{SrBO_2F}\right| = 2.68 \times KDP$$

for $BaBO_2F$:

$$\left|d_{22}^{BaBO_2F}\right| = 3.04 \times KDP,$$

$$\left|d_{23}^{BaBO_2F}\right| = \left|d_{34}^{BaBO_2F}\right| = 2.85 \times KDP$$

Thus, the calculated values for both materials can be considered as excellent, especially the d_{22} component, which is three times higher than d_{36} of KDP for both structures.

To analyze the origin of the large SHG coefficients, we adopted the real-space atom-cutting method [43]. Following its core principle, the real space of $SrBO_2F$ and $BaBO_2F$ was divided into spherical zones centered on each ion (Sr/Ba, B, O, F). The cutting radius of each zone was determined by the local charge density minimum between adjacent ions, ensuring non-overlapping contact for accurate contribution separation. For cutting radius parameterization: In $SrBO_2F$, Sr's radius was 1.13 Å (from Sr-O charge density distribution), O's was 1.11 Å (to avoid overlap with Sr), and F's was 1.04 Å. A B-cutoff radius equal to its covalent radius (0.88 Å) was adopted to strictly confine the atomic cutting sphere of B, thereby preventing spatial overlap with the neighboring O atoms of the $[BO_2]_\infty$ chain and ensuring that the chain's contribution to the SHG response is accurately and independently evaluated. For $BaBO_2F$ Ba's radius followed the same charge density criterion as Sr, determined to be 1.35 Å, with O, B, F radii consistent with $SrBO_2F$ (O: 1.11 Å, B: 0.88 Å, F: 1.04 Å) for comparability. By cutting ion/cluster wave functions and calculating remaining SHG coefficients, we extracted individual contributions. Results show SHG in $SrBO_2F$ and $BaBO_2F$ is dominated by $[BO_2]_\infty$ infinite chains (97% and 98% contributions, respectively), with negligible contributions from Sr/Ba and F (<3%). This indicates that the $[BO_2]_\infty$ chain is an excellent anionic framework for nonlinear optical materials. This conclusion is confirmed by studies of other borates that contain similar units. For example, crystals $LiBO_2$ and Li_2BO_2F which contain $[BO_2]_\infty$ chains exhibit deep UV transparency (<177.3 nm), show a large NLO response (2.0-2.3 x KH_2PO_4) and large birefringence (0.093-0.146 at $\lambda = 1064$ nm) [44,45]. Consequently, the $[BO_2]_\infty$ chain is validated as a leading anionic functional unit for the design of optical materials, capable of demonstrating strong nonlinear optical responses and excellent linear optical properties.

To further validate the potential of $SrBO_2F$ and $BaBO_2F$ for deep-ultraviolet (DUV) nonlinear optical applications, we compare their key properties: UV cutoff edge, nonlinear optical coefficient, and birefringence with those of well-established DUV NLO crystals, including KBBF ($KBe_2BO_3F_2$), RBBF ($RbBe_2BO_3F_2$), CBBF ($CsBe_2BO_3F_2$), ABF ($NH_4B_4O_6F$), LBO (LiB_3O_5), BBO (BaB_2O_4), and CBF (CsB_4O_6F).

The KBBF-family crystals represent the current DUV benchmark. KBBF exhibits a cutoff edge at 147 nm, a nonlinear coefficient of 0.47 p.m./V, and a birefringence of 0.0853 [11]. Its analogues RBBF and CBBF show cutoff edges at 152 nm and 151 nm, birefringence values of 0.0752 and 0.0616, and nonlinear coefficients of 0.45 and 0.50 p.m./V, respectively [46]. Among beryllium-free alternatives, ABF shows a cutoff at 156 nm, a birefringence of 0.1171, and a nonlinear coefficient of 1.19 p.m./V [13]. CBF exhibits a cutoff at 155 nm, a large NLO response of 0.73 p.m./V, and a birefringence of 0.1137 [47]. BBO has a cutoff at 189 nm, a nonlinear coefficient of 2.12 p.m./V and a birefringence of 0.12 [41], whereas LBO has cutoff at 158 nm, a nonlinear coefficient of 0.83 p.m./V and a birefringence of 0.04 [48].

The band gaps of our $SrBO_2F$ and $BaBO_2F$ materials are 6.73 eV and 6.35 eV, respectively, and the corresponding cutoff edges are 184 nm and 195 nm. Their birefringence values of 0.087 and 0.077 are very close to those of KBBF (0.0853) and RBBF (0.0752) and are well within the optimal range of 0.05–0.10 for DUV phase matching. The nonlinear coefficients of 1.16 p.m./V and 1.17 p.m./V exceed the values of the KBBF-family and are similar to that of the ABF crystal.

All these comparisons together show that the predicted $SrBO_2F$ and $BaBO_2F$ possess a good balance of wide DUV transparency, sufficiently large birefringence and strong SHG response. This positions them as particularly attractive candidates for replacing toxic beryllium-containing DUV NLO materials such as KBBF.

4. Conclusions

The predicted borate fluorides compounds $SrBO_2F$ and $BaBO_2F$ are low-energy metastable materials with favorable optical properties. Their crystal structures, combining layers of $[M^{+2}O_4F_4]$, $[MF_8]$ and $[MO_8]$

Table 1
Calculated properties of the predicted $SrBO_2F$ and $BaBO_2F$. Unit cell parameters were obtained within the PBE functional. The cutoff edge λ_{cutoff}, birefringence Δn, and phase matching wavelengths λ_{PM} were calculated assuming the band gap value obtained within the HSE06 functional.

Chemical composition	Space group	Conventional cell parameters	Primitive cell parameters	$E_{g,\ indirect}$ (HSE06), eV	λ_{cutoff}, nm	Δn	λ_{PM}, nm	$\lvert d_{22}\rvert$, pm/V
$SrBO_2F$	$C2$	$a = 6.92$ Å $b = 4.34$ Å $c = 18.96$ Å $\alpha = \gamma = 90.0°$ $\beta = 97.3°$	$a = b = 4.09$ Å $c = 18.96$ Å $\alpha = \beta = 96.1°$ $\gamma = 64.2°$	6.73	184	0.087	197	1.16
$BaBO_2F$	$C2$	$a = 7.52$ Å $b = 4.46$ Å $c = 19.97$ Å $\alpha = \gamma = 90.0°$ $\beta = 97.2°$	$a = b = 4.37$ Å $c = 19.97$ Å $\alpha = \beta = 96.2°$ $\gamma = 61.3°$	6.35	195	0.077	222	1.17

polyhedra and $[BO_2]_\infty$ chains of interconnected planar $[BO_3]$ units, lead to the reduced dimensionality of their phonon and electronic bands. Most of the valence bands of these materials exhibit a two-dimensional character, with no dispersion along the direction, perpendicular to the layer's surface. Some of the valence bands, corresponding to the orbitals of the $[BO_2]_\infty$ chains, are rather one-dimensional. The structure of these materials induces non-centrosymmetric polarization and significant optical anisotropy, resulting in strong SHG responses and birefringence suitable for phase-matched nonlinear optical processes. The predicted main properties of the obtained materials are summarized in Table I. The real-space atom-cutting analysis shows that the frequency doubling in $SrBO_2F$ and $BaBO_2F$ predominantly originates from the $[BO_2]_\infty$ chains (97% and 98%, respectively), confirming their role as an excellent anionic framework for nonlinear optical applications. The one-dimensional $[BO_2]_\infty$ chain thus emerges as a highly effective anionic functional unit for NLO design, simultaneously enabling strong SHG response and sufficient birefringence for phase matching. With deep-UV transparency extending below 200 nm, these compounds are well-suited for DUV applications.

The computational prediction of $SrBO_2F$ and $BaBO_2F$ crystals with promising nonlinear optical properties demonstrates that the Ae-B-O-F systems have high potential as possible sources of novel nonlinear borate fluoride materials. The proposed computational approach may be extended to other compositions within these systems to provide a broader understanding of the influence of the chemical composition of the borate fluorides on their structural stability and nonlinear optical properties.

CRediT authorship contribution statement

Daria D. Barma: Data curation, Formal analysis, Investigation, Methodology, Validation, Writing – original draft. **Andrey S. Obrubov:** Visualization. **Abudukadi Tudi:** Conceptualization, Resources, Validation. **Zhihua Yang:** Conceptualization, Resources, Validation. **Anastasiia A. Mikhailova:** Formal analysis, Methodology, Resources, Software, Writing – review & editing. **Dmitry V. Rybkovskiy:** Conceptualization, Data curation, Formal analysis, Investigation, Methodology, Project administration, Validation. **Artem R. Oganov:** Conceptualization, Funding acquisition, Project administration, Resources, Supervision, Writing – review & editing.

Declaration of competing interest

The authors declare that they have no known competing financial interests or personal relationships that could have appeared to influence the work reported in this paper.

Acknowledgements

The work was funded by Russian Science Foundation grant N⁰ 24-43-00162. The calculations were performed on Oleg and Arkuda supercomputers at Skoltech, the Lobachevsky cluster at the University of Nizhny Novgorod and the heterogeneous computing platform HybriLIT (LIT, JINR).

Appendix A. Supplementary data

Supplementary data to this article can be found online at https://doi.org/10.1016/j.cocom.2026.e01417.

Data availability

The data supporting the findings of this study are available in the Supplementary Information (POSCAR, CIF-files)

References

[1] P.R. Herman, R.S. Marjoribanks, A. Oettl, K. Chen, I. Konovalov, S. Ness, Laser shaping of photonic materials: deep-ultraviolet and ultrafast lasers, Appl. Surf. Sci. 154 (155) (Feb. 2000) 577–586, https://doi.org/10.1016/S0169-4332(99)00463-8.
[2] Z. Xu, B.M. Sadler, Ultraviolet communications: potential and state-of-the-art, IEEE Commun. Mag. 46 (5) (May 2008) 67–73, https://doi.org/10.1109/MCOM.2008.4511651.
[3] K.S.E. Eikema, W. Ubachs, Precision Laser spectroscopy in the extreme ultraviolet, in: M. Quack, F. Merkt (Eds.), Handbook of High-Resolution Spectroscopy, first ed., Wiley, 2011 https://doi.org/10.1002/9780470749593.hrs079.
[4] E.A. Boardman, L.S.-W. Huang, J.J. Robson-Hemmings, T.M. Smeeton, S. E. Hooper, J. Heffernan, Deep Ultraviolet (UVC) Laser for Sterilisation and Fluorescence Applications, 104, 2012, pp. 31–35.
[5] V. Panov, T. Borisova-Papancheva, Application of ultraviolet light (UV) in dental medicine, J. Med. Dent. Pract. 2 (2) (Jul. 2015) 194–200, https://doi.org/10.18044/MedInform.201522.194.
[6] R. Paetzel, Comparison excimer laser – solid state laser. Presented at the ICALEO 2002: 21St International Congress on Laser Materials Processing and Laser Microfabrication, AIP Publishing, Oct. 2002, https://doi.org/10.2351/1.5066151.
[7] B. Zhang, E. Tikhonov, C. Xie, Z. Yang, S. Pan, Prediction of fluorooxoborates with colossal Second Harmonic Generation (SHG) coefficients and extremely wide band gaps: towards modulating properties by tuning the BO_3/BO_3F ratio in layers, Angew. Chem. 58 (34) (Aug. 2019) 11726–11730, https://doi.org/10.1002/anie.201905558.
[8] A. Tudi, S. Han, Z. Yang, S. Pan, Band-Gap modulation of nonlinear-optical fluorooxoborates by controlling the F/B ratios, Inorg. Chem. 59 (3) (Feb. 2020) 1588–1591, https://doi.org/10.1021/acs.inorgchem.9b03419.
[9] Y. Alkabakibi, D.D. Barma, D.V. Rybkovskiy, A. Tudi, C. Xie, A.R. Oganov, Computational identification of four promising nonlinear optical materials for near and middle ultraviolet operation, JETP Lett. 121 (4) (Feb. 2025) 256–261, https://doi.org/10.1134/S0021364024605074.
[10] J. Lin, M.-H. Lee, Z.-P. Liu, C. Chen, C.J. Pickard, Mechanism for linear and nonlinear optical effects in β-BaB_2O_4 crystals, Phys. Rev. B 60 (Nov. 1999) 13380–13389, https://doi.org/10.1103/PhysRevB.60.13380.
[11] D. Tang, Y. Xia, B. Wu, C. Chen, Growth of a new UV nonlinear optical crystal:: $KBe_2(BO_3)F_2$, J. Cryst. Growth 222 (1) (Jan. 2001) 125–129, https://doi.org/10.1016/S0022-0248(00)00850-2.
[12] C. Chen, et al., Deep UV nonlinear optical crystal:$RbBe_2(BO_3)F_2$, JOSA B 26 (8) (Aug. 2009) 1519–1525, https://doi.org/10.1364/JOSAB.26.001519.
[13] G. Shi, et al., Finding the next deep-ultraviolet nonlinear optical material: $NH_4B_4O_6F$, J. Am. Chem. Soc. 139 (31) (Aug. 2017) 10645–10648, https://doi.org/10.1021/jacs.7b05943.
[14] H. Liu, H. Wu, Z. Hu, J. Wang, Y. Wu, H. Yu, $Cs_3[(BOP)_2(B_3O_7)_3]$: a deep-ultraviolet nonlinear optical crystal designed by optimizing matching of cation and anion groups, J. Am. Chem. Soc. 145 (23) (Jun. 2023) 12691–12700, https://doi.org/10.1021/jacs.3c02400.

[15] M. Mutailipu, et al., Achieving the full-wavelength phase-matching for efficient nonlinear optical frequency conversion in $C(NH_2)_3BF_4$, Nat. Photonics 17 (8) (Aug. 2023) 694–701, https://doi.org/10.1038/s41566-023-01228-7.

[16] Z. Lin, Z. Wang, C. Chen, S.K. Chen, M.-H. Lee, Mechanism for linear and nonlinear optical effects in crystals of the $Sr_2Be_2B_2O_7$ family, J. Appl. Phys. 93 (12) (Jun. 2003) 9717–9723, https://doi.org/10.1063/1.1577816.

[17] M. Mutailipu, K.R. Poeppelmeier, S. Pan, Borates: a rich source for optical materials, Chem. Rev. 121 (3) (Feb. 2021) 1130–1202, https://doi.org/10.1021/acs.chemrev.0c00796.

[18] C. Huang, F. Zhang, H. Li, Z. Yang, H. Yu, S. Pan, $BaB_2O_3F_2$: a barium fluorooxoborate with a unique $^{\infty}_{2}[B_2O_3F]^-$ layer and short cutoff edge, Chemistry 25 (27) (May 2019) 6693–6697, https://doi.org/10.1002/chem.201806350.

[19] C.D. McMillen, J.T. Stritzinger, J.W. Kolis, Two novel acentric Borate fluorides: $M_3B_6O_{11}F_2$ (M = Sr, Ba), Inorg. Chem. 51 (7) (Apr. 2012) 3953–3955, https://doi.org/10.1021/ic202318b.

[20] H. Wu, et al., Top-Seeded solution crystal growth and Linear and nonlinear optical properties of $Ba_4B_{11}O_{20}F$, Cryst. Growth Des. 17 (3) (Mar. 2017) 1404–1410, https://doi.org/10.1021/acs.cgd.6b01857.

[21] M. Mutailipu, et al., $SrB_5O_7F_3$ functionalized with $[B_5O_9F_3]^{6-}$ chromophores: accelerating the rational design of deep-ultraviolet nonlinear optical materials, Angew. Chem. 57 (21) (May 2018) 6095–6099, https://doi.org/10.1002/anie.201802058.

[22] A.R. Oganov, C.W. Glass, Crystal structure prediction using ab initio evolutionary techniques: principles and applications, J. Chem. Phys. 124 (24) (Jun. 2006) 244704, https://doi.org/10.1063/1.2210932.

[23] H. Yang, et al., MatterSim: a deep learning atomistic model across elements, temperatures and pressures, arXiv: arXiv:2405.04967 (May 10, 2024), https://doi.org/10.48550/arXiv.2405.04967.

[24] J. Hafner, Ab-initio simulations of materials using VASP: Density-functional theory and beyond, J. Comput. Chem. 29 (13) (2008) 2044–2078, https://doi.org/10.1002/jcc.21057.

[25] G.K.H. Madsen, Functional form of the generalized gradient approximation for exchange: the PBEα functional, Phys. Rev. B 75 (19) (May 2007) 195108, https://doi.org/10.1103/PhysRevB.75.195108.

[26] A. Jain, et al., Commentary: the Materials Project: a materials genome approach to accelerating materials innovation, APL Mater. 1 (1) (Jul. 2013) 11002, https://doi.org/10.1063/1.4812323.

[27] A. Togo, K. Shinohara, I. Tanaka, Spglib: a software library for crystal symmetry search, Sci. Technol. Adv. Mater. Methods 4 (1) (Dec. 2024) 2384822, https://doi.org/10.1080/27660400.2024.2384822.

[28] M. Gajdoš, K. Hummer, G. Kresse, J. Furthmüller, F. Bechstedt, Linear optical properties in the projector-augmented wave methodology, Phys. Rev. B 73 (4) (Jan. 2006) 45112, https://doi.org/10.1103/PhysRevB.73.045112.

[29] A.V. Krukau, O.A. Vydrov, A.F. Izmaylov, G.E. Scuseria, Influence of the exchange screening parameter on the performance of screened hybrid functionals, J. Chem. Phys. 125 (22) (Dec. 2006) 224106, https://doi.org/10.1063/1.2404663.

[30] A.H. Romero, et al., ABINIT: overview and focus on selected capabilities, J. Chem. Phys. 152 (12) (Mar. 2020) 124102, https://doi.org/10.1063/1.5144261.

[31] M. Veithen, X. Gonze, Ph Ghosez, Nonlinear optical susceptibilities, Raman efficiencies, and electro-optic tensors from first-principles density functional perturbation theory, Phys. Rev. B 71 (12) (Mar. 2005) 125107, https://doi.org/10.1103/PhysRevB.71.125107.

[32] X. Gonze, J.-P. Vigneron, Density-functional approach to nonlinear-response coefficients of solids, Phys. Rev. B 39 (18) (Jun. 1989) 13120–13128, https://doi.org/10.1103/PhysRevB.39.13120.

[33] M.J. van Setten, et al., The PseudoDojo: training and grading a 85 element optimized norm-conserving pseudopotential table, Comput. Phys. Commun. 226 (May 2018) 39–54, https://doi.org/10.1016/j.cpc.2018.01.012.

[34] P. Giannozzi, et al., Quantum ESPRESSO: a modular and open-source software project for quantum simulations of materials, J. Phys. Condens. Matter 21 (39) (Sep. 2009) 395502, https://doi.org/10.1088/0953-8984/21/39/395502.

[35] B. Cheng, et al., $(NH_4)_3B_{11}PO_{19}F_3$: a deep-UV nonlinear optical crystal with unique $[B_5PO_{10}F]\infty$ layers, Natl. Sci. Rev. 9 (8) (Aug. 2022) nwac110, https://doi.org/10.1093/nsr/nwac110.

[36] T. Christensen, *thchr/Brillouin.jl*. (Mar. 19, 2026). Julia. https://github.com/thchr/Brillouin.jl. (Accessed 10 July 2026).

[37] L. Mei, Y. Wang, C. Chen, Crystal structure of sodium beryllium borate fluoride, Mater. Res. Bull. 29 (1) (Jan. 1994) 81–87, https://doi.org/10.1016/0025-5408(94)90108-2.

[38] J. Shen, P.B. Moore, Crystal structure of cappelenite, $Ba(Y,RE)_6[Si_3Be_6O_{24}]F_2$: a siliceborate sheet structure, Am. Mineral. 69 (1–2) (1984) 190–195.

[39] A. Perloff, S. Block, The crystal structure of the strontium and lead tetraborates, $SrO.2B_2O_3$ and $PbO.2B_2O_3$, Acta Crystallogr. 20 (2) (Feb. 1966) 274–279, https://doi.org/10.1107/S0365110X66000525.

[40] W. Zhang, H. Yu, H. Wu, P.S. Halasyamani, Phase-Matching in nonlinear optical compounds: a materials perspective, Chem. Mater. 29 (7) (Apr. 2017) 2655–2668, https://doi.org/10.1021/acs.chemmater.7b00243.

[41] S. Solgi, M.J. Tafreshi, M.S. Ghamsari, Nonlinear optical crystals for second harmonic generation, Crystallogr. Rep. 64 (7) (Dec. 2019) 1138–1149, https://doi.org/10.1134/S1063774519070204.

[42] W. Yao, R. He, X. Wang, Z. Lin, C. Chen, Analysis of Deep-UV nonlinear optical borates: approaching the end, Adv. Opt. Mater. 2 (5) (2014) 411–417, https://doi.org/10.1002/adom.201300535.

[43] Z. Lin, J. Lin, Z. Wang, C. Chen, M.-H. Lee, Mechanism for linear and nonlinear optical effects in LiB_3O_5, CsB_3O_5, and $CsLiB_6O_{10}$ crystals, Phys. Rev. B 62 (3) (Jul. 2000) 1757–1764, https://doi.org/10.1103/PhysRevB.62.1757.

[44] A. Tudi, C. Xie, S. Pan, Z. Yang, Design of novel deep-UV nonlinear optical materials with one-dimensional functional module $[BO_2]_\infty$ chain and fluorine-driven short phase-matching, Mater. Today Phys. 28 (Nov. 2022) 100852, https://doi.org/10.1016/j.mtphys.2022.100852.

[45] Y. Wang, E. Tikhonov, H. Niu, Prediction of promising deep ultraviolet nonlinear optical materials in the Li_2O–B_2O_3 System, Chem. Mater. 35 (11) (Jun. 2023) 4201–4210, https://doi.org/10.1021/acs.chemmater.3c00081.

[46] L. Kang, S. Luo, H. Huang, T. Zheng, Z.S. Lin, C.T. Chen, Ab initio studies on the optical effects in the deep ultraviolet nonlinear optical crystals of the $KBe_2BO_3F_2$ family, J. Phys. Condens. Matter 24 (33) (Jul. 2012) 335503, https://doi.org/10.1088/0953-8984/24/33/335503.

[47] X. Wang, Y. Wang, B. Zhang, F. Zhang, Z. Yang, S. Pan, CsB_4O_6F: a congruent-melting deep-ultraviolet nonlinear optical material by combining superior functional units, Angew. Chem. 129 (45) (2017) 14307–14311, https://doi.org/10.1002/ange.201708231.

[48] D.N. Nikogosyan, Lithium triborate (LBO), Appl. Phys. A 58 (3) (Mar. 1994) 181–190, https://doi.org/10.1007/BF00324374.